**APPLIED SCIENCES AND ENGINEERING**

# A 10-micrometer-thick nanomesh-reinforced gas-permeable hydrogel skin sensor for long-term electrophysiological monitoring

Zongman Zhang[1,2], Jiawei Yang[1,2], Haoyang Wang[3], Chunya Wang[4]*, Yuheng Gu[1,2], Yumiao Xu[1,2], Sunghoon Lee[3], Tomoyuki Yokota[3], Hossam Haick[2], Takao Someya[3]*, Yan Wang[1,2,5,6]*

Hydrogel-enabled skin bioelectronics that can continuously monitor health for extended periods is crucial for early disease detection and treatment. However, it is challenging to engineer ultrathin gas-permeable hydrogel sensors that can self-adhere to the human skin for long-term daily use (>1 week). Here, we present a ~10-micrometer-thick polyurethane nanomesh–reinforced gas-permeable hydrogel sensor that can self-adhere to the human skin for continuous and high-quality electrophysiological monitoring for 8 days under daily life conditions. This research involves two key steps: (i) material design by gelatin-based thermal-dependent phase change hydrogels and (ii) robust thinness geometry achieved through nanomesh reinforcement. The resulting ultrathin hydrogels exhibit a thickness of ~10 micrometers with superior mechanical robustness, high skin adhesion, gas permeability, and anti-drying performance. To highlight the potential applications in early disease detection and treatment that leverage the collective features, we demonstrate the use of ultrathin gas-permeable hydrogels for long-term, continuous high-precision electrophysiological monitoring under daily life conditions up to 8 days.

## INTRODUCTION

Skin bioelectronics capable of long-term, continuous health monitoring offers a powerful route for timely disease prevention, screening, diagnosis, and treatment in personalized health care (1–3). Hydrogels, as a group of cross-linked polymers with high water content, have gained considerable attention in skin bioelectronics by virtue of their similarities to biological tissues and versatility in electrical, mechanical, and biofunctional engineering (4–6). Hydrogel-enabled skin bioelectronic devices have seen tremendous health care applications (7, 8), such as biometric signals detection (9), human-machine interfaces (10), wound healing (11), and precision therapy (12). Hydrogel skin sensors that can sustain prolonged skin attachment and high-fidelity health monitoring can enable early disease diagnosis and timely therapy interventions (1, 13).

To ensure reliable, long-term, and continuous health monitoring, hydrogel bioelectronics should first overcome intrinsic issues such as easy dehydration and mechanical softness (14). Hydrogels tend to dry out when exposed in an open-air environment for a certain period of time due to their high water content, thus shortening their service life (15). There has been important progress made to bolster their anti-drying capability and mechanical strength (16, 17). For example, promising strategies such as solvent replacement and the addition of highly hydrated salts have been widely used to fabricate anti-drying hydrogel skin sensors (18). Wang *et al.* (19) reported a gelatin-based hydrogel sensor that could acquire high-fidelity electroencephalogram (EEG) signals over 3 days using a glycerol/water binary solvent system for long-term stability. Meanwhile, approaches such as double networks (20) and fiber reinforcement (21) have been extensively exploited to construct mechanically durable hydrogel bioelectronics. An example of this is an ultrathin (<5-μm-thick) microfiber composite hydrogel that has a tensile stress of ~6 MPa and high anti-tearing properties (22). The recording of high-quality electromyogram (EMG) remained stable after storage under an ambient environment for over 10 days. Other prerequisites of reliable, long-term, continuous health monitoring include high skin conformability and gas permeability (23, 24). Great skin conformability is a critical factor in realizing low skin contact impedance (25). An effective method to construct hydrogels with a high skin adhesion is to incorporate catechol-containing compounds, such as polydopamine, tannic acid, and tea polyphenols, in the hydrogel matrix (26). For instance, a semidry double-layer hydrogel could bond to the human skin for 12 hours continuous high-quality EEG monitoring due to its high adhesiveness and anti-drying properties (27). It should be noted that most existing adhesive conductive hydrogels are thick and bulky, leading to inferior gas permeability. Considering that the human skin is losing sensible and insensible sweat constantly (~600 g m$^{-2}$ day$^{-1}$) (28), covering the human skin with insufficiently gas-permeable materials leads to serious health concerns, such as irritation, allergy, and inflammation (28, 29). By decreasing the thickness to sub–10 μm, the hydrogels exhibited great skin compliance and a high water vapor transmission rate (WVTR) of 1890.0 ± 134.4 g m$^{-2}$ day$^{-1}$ for a 7-day skin wear (30). This research further demonstrated high feasibility of 10-μm-thick hydrogel-interfaced flexible organic (opto)electronics (e.g., field-effect transistors, electrochemical transistors, and photovoltaics) attached to the human skin for biosignal monitoring.

However, it has been challenging to engineer ultrathin gas-permeable hydrogel sensors that can self-adhere to the human skin for more

[1]Department of Chemical Engineering, Guangdong Technion-Israel Institute of Technology, 241 Daxue Road, Shantou, Guangdong 515063, China. [2]The Wolfson Department of Chemical Engineering, Technion-Israel Institute of Technology, Haifa 3200003, Israel. [3]Department of Electrical Engineering and Information Systems, The University of Tokyo, 7-3-1 Bunkyo-ku, Tokyo 112-8656, Japan. [4]State Key Laboratory of Heavy Oil Processing, College of Carbon Neutrality Future Technology, China University of Petroleum (Beijing), Beijing 102249, China. [5]Guangdong Provincial Key Laboratory of Materials and Technologies for Energy Conversion, Guangdong Technion-Israel Institute of Technology, 241 Daxue Road, Shantou, Guangdong 515063, China. [6]Guangdong Provincial Key Laboratory of Science and Engineering for Health and Medicine, Guangdong Technion-Israel Institute of Technology, Shantou, Guangdong 515063, China.
*Corresponding author. Email: chunyawang@cup.edu.cn (C.W.); someya@ee.t.u-tokyo.ac.jp (T.S.); yan.wang@gtiit.edu.cn (Y.W.)

than a week of daily use. These sensors must not only be ultrathin and gas-permeable but also adhesive, robust, and capable of preventing dryness. First, it is difficult to prepare micrometer-scale-thick hydrogels with high gas permeability, skin adhesiveness, and mechanical robustness. Although it is possible to fabricate ultrathin, gas-permeable, and self-adhesive hydrogels (30), there exists a scarcity of publications addressing ultrathin hydrogels because of the challenges in fabrication techniques and manipulation (22, 30). In addition, hydrogels with micrometer-scale thickness are generally vulnerable to mechanical disruptions owing to their sacrificed mechanical robustness. The improvement of mechanical properties usually results in thick devices that severely limit gas permeability and cause mechanical or sensation interferences (31, 32). Furthermore, another nonignorable concern is the intrinsic easy-dehydration behavior of hydrogels that leads to signal deterioration during prolonged monitoring (19, 33, 34). It is worth noting that thinner hydrogels tend to have accelerated drying rates due to the higher surface area–to–volume ratio. On the basis of the summary of recently reported gas-permeable and/or anti-drying hydrogel-enabled skin bioelectronics (table S1) (6, 15, 22, 27, 30, 35–41), it can be concluded that hydrogel skin bioelectronics capable of long-term, continuous health monitoring under daily life conditions (>1 week) have not been reported yet.

In this work, we have succeeded in developing a 10-μm-thick polyurethane (PU) nanomesh–reinforced gas-permeable hydrogel sensor that can self-adhere to the human skin for continuous and high-quality electrophysiological monitoring for 8 days under daily life conditions. This research involves two key steps: (i) material design by gelatin-based thermal-dependent phase change hydrogels and (ii) robust thinness geometry by nanomesh reinforcement. The ultrathin, reinforced structure is readily achieved by dipping PU nanomeshes into a temperature-dependent phase transition hydrogel solution (Fig. 1A). The resulting ultrathin hydrogels exhibit a thickness of ~10 μm with superior mechanical robustness (tensile stress of 2.5 MPa, stretchability of up to 696% strain, and 1000 cyclic stretching to 100% strain), high skin adhesion (an area adhesion energy of 176.8 μJ cm$^{-2}$), gas permeability (1669.3 g m$^{-2}$ day$^{-1}$), and anti-drying performance (12-day skin wear). We successfully demonstrate long-term and high-fidelity recording of electrocardiogram (ECG), EMG, motor conduction velocity (MCV), electrooculogram (EOG), EEG, auditory brainstem response (ABR), and visual evoked potential (VEP) signals using the ultrathin and gas-permeable hydrogels (Fig. 1B).

The long-term electrophysiological sensing performance of the hydrogel is maintained over continuous wearing under daily life conditions due to the combination of key attributes. These attributes include its ultrathin structure, exceptional mechanical properties, gas permeability, self-adhesiveness, and anti-drying capabilities. The ultrathin structure is achieved by dip-coating electrospun nanomeshes into a diluted gelatin hydrogel solution at a high temperature (55° to 75°C) and then gelating at a physiological temperature or under ambient environment. The nanomesh reinforcement significantly bolsters the mechanical durability of the ultrathin hydrogel. The gas permeability is attributed to the thinness geometry and porous nature of the hydrogel. In addition, the thinness also contributes to its self-adhesiveness; another reason for high self-adhesiveness is the strong and reversible chemical and physical bonds formed at the hydrogel-skin interface. Furthermore, the anti-drying capability is improved by the introduction of glycerol/water binary solvent and hydrated salt into its composition.

## RESULTS

### Design and characterization of the ultrathin yet mechanically robust hydrogels

To overcome the mechanical robustness-thinness geometry dilemma, nanomesh reinforcement has been proven to be an effective approach to fabricate robust polymeric nanofilms (42). Here, PU nanomeshes were chosen as a reinforcement layer fabricated via electrospinning (fig. S1). To realize the proposed hydrogel design, gelatin was chosen as the main matrix of hydrogels owing to its triple helix structure, which undergoes a phase transition between gel and liquid states determined by temperature (19). The ultrathin-reinforced hydrogel was achieved by dip-coating electrospun nanomeshes (density of 0.3 mg cm$^{-2}$) into a diluted gelatin hydrogel solution at a high temperature (55° to 75°C) and then gelating at a physiological temperature or under ambient environment (see detailed fabrication process in fig. S2). The cross-sectional scanning electron microscopy (SEM) image demonstrates a 10.3-μm-thick reinforced hydrogel adhered on an anodisc substrate (Fig. 1C). By decreasing the thickness to ~10 μm, the hydrogel can (i) significantly increase skin compliance by reducing flexural rigidity and (ii) allows fast gas/vapor diffusion from the skin underneath. To our surprise, the freely suspended ultrathin hydrogel could support large amounts of water that are 248 times heavier than its own weight, with a tensile stress of 2.5 MPa (Fig. 1D, fig. S3, and movie S1). The ultrathin robust hydrogels also exhibit fast and reversible adhesion to the human skin, allowing repetitive dynamic adhesion to the human skin similar to an adhesive tape (Fig. 1E and movie S2).

For the design of hydrogel material, borax was used as the cross-linking agent, which can dissociate into borate ions and boric acid and react with gelatin and glycerol to form intertwined network structures (43). In addition, borax can improve the cross-linking density, thereby adjusting the transition temperature of the hydrogels. As depicted in fig. S4 and movie S3, the PU nanomesh–reinforced hydrogel with a borax content of 1.5 g exhibits the highest stretchability of 606% strain. In addition, the as-developed hydrogel shows long-lasting anti-drying performance by introducing glycerol/water binary solvent (44). The anti-drying performance enhanced with the increased content of glycerol while resulting in higher intrinsic impedance (fig. S5). The electrical performance of PU nanomesh–reinforced hydrogels with varied sodium sulfate (Na$_2$SO$_4$) content was examined. The results show that the hydrogels with a higher content of Na$_2$SO$_4$ exhibited a lower intrinsic impedance but led to a salting out of Na$_2$SO$_4$ after 12-hour storage under an ambient environment (fig. S6). The hydrogels with optimized glycerol, borax, and Na$_2$SO$_4$ of 8.0, 1.5, and 1.3 g, respectively, were chosen for further experiments. The hydrogel made of gelatin, borax, glycerol, and Na$_2$SO$_4$, is denoted as "GGBWNa." GGBWNa hydrogel made from PU nanomeshes with a density of 0.3 mg cm$^{-2}$ is here referred to as "ultrathin hydrogel" unless otherwise specified.

To verify the thermally responsive liquid-gel transition features of the hydrogel materials, photographs and infrared camera images were taken at high (55°C) and room (25°C) temperatures (Fig. 2A). The results show that the hydrogels could transform into a liquid state at 55°C and a gel state at 25°C. The rheological experiment was performed to confirm the conclusion (45) by comparing borax-free hydrogels (GGWNa) and GGBWNa hydrogels (Fig. 2B). The storage modulus $G'$ and loss modulus $G''$ of GGWNa and GGBWNa hydrogels gradually increase with decreasing temperature. During cooling process, the corresponding tanδ ($G''/G'$) of GGWNa and GGBWNa
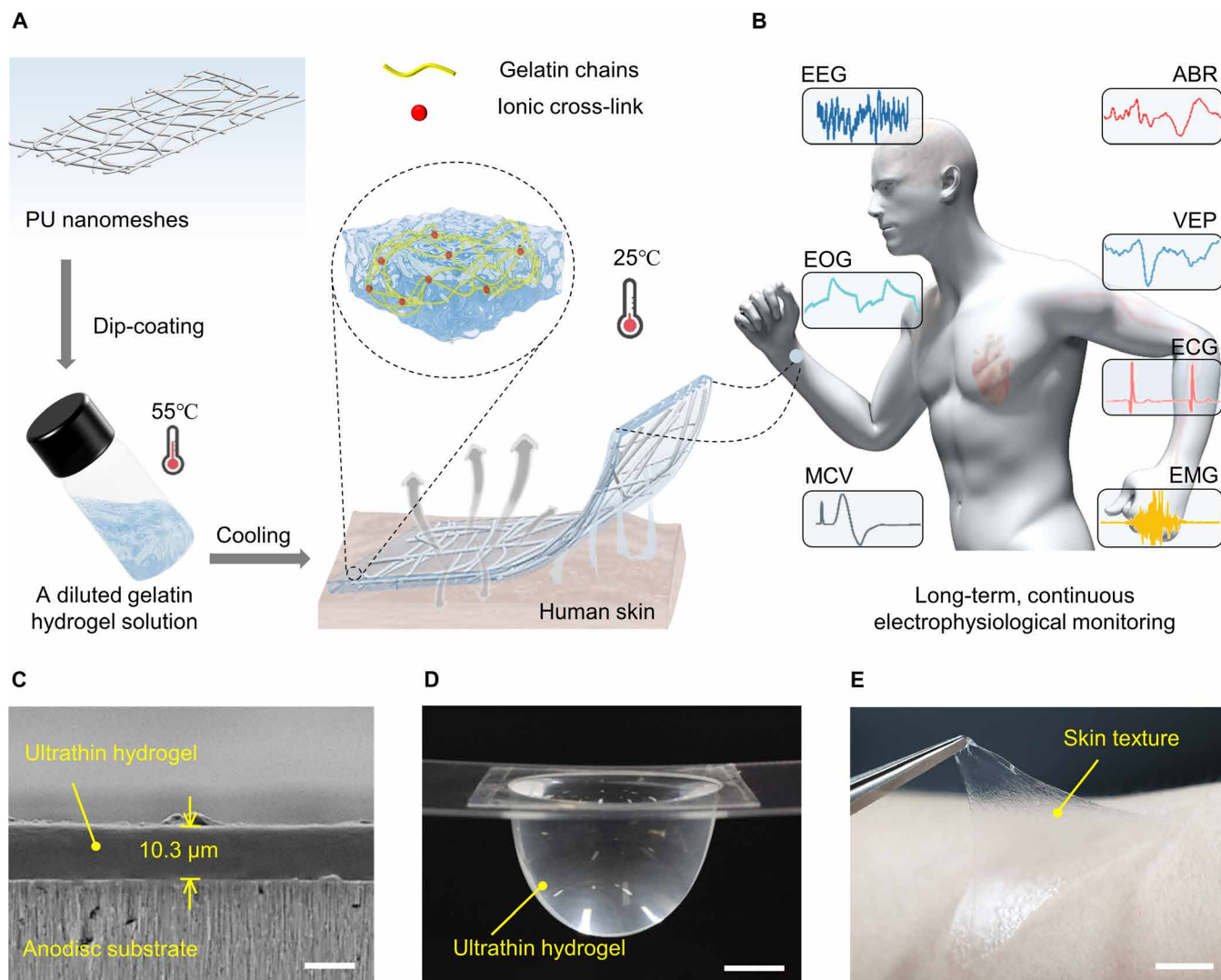
**Fig. 1. A 10-μm-thick nanomesh-reinforced hydrogel for long-term, continuous electrophysiological monitoring.** (**A**) Schematic illustration of the design concept of PU nanomesh–reinforced hydrogels. (**B**) Ultrathin hydrogel used for long-term, continuous electrophysiological monitoring, such as ECG, EMG, MCV, EOG, EEG, ABR, and VEP. (**C**) Cross-sectional SEM image of the ultrathin hydrogel attached on an anodisc substrate. Scale bar, 10 μm. (**D**) A photograph of a suspended ultrathin hydrogel holding a large amount of water. The tensile stress (σ) can be calculated by dividing the body force of the liquids by the thickness and circumference of the ultrathin hydrogels: $\sigma = \frac{Pr}{2t}$, where the $P$, $r$, and $t$ are the applied pressure of the water, the radius of the curvature, and the thickness of the ultrathin hydrogels, respectively (*42*). Scale bar, 1 cm. (**E**) A photograph of the peeling-off of an ultrathin hydrogel from the human skin, showing strong adhesion and high elasticity. Scale bar, 1 cm.

hydrogels decreased to less than 1 at ~37.0° and ~41.0°C, respectively, denoting their transition temperatures from viscous liquid to viscoelastic gel state (Fig. 2C). The increased transition temperature of GGBWNa hydrogels corresponds to the higher cross-linking density induced by borax, meaning that GGBWNa hydrogels are more suitable for skin applicability. During the heating process, the tanδ ($G''/G'$) of GGWNa and GGBWNa hydrogels exhibited an escalating trend with a value of more than 1 when the temperature was larger than 44°C, signifying the reversible phase transition from gel to liquid state at high temperatures (fig. S7). The temperature-dependent transition between viscous liquid and viscoelastic gel states is attributed to the thermo-induced destruction and reconstruction of the physical interactions in the hydrogel matrix. Fourier transform infrared (FTIR) spectrum test was further conducted to study hydrogels with varied components (Fig. 2D). The characteristic

absorption band at 3340 and 1643 cm$^{-1}$ is related to the O—H stretching vibration and hydrogen bond vibration, respectively. In addition, the absorption peaks at 1070 cm$^{-1}$ belong to the asymmetry extension of B—O—C bond, indicating the cross-linking by borax (*43*).

The as-developed ultrathin hydrogel exhibits a high transmittance of 87% at a 550-nm wavelength. The insert photograph in Fig. 2E depicts the high transparency of the ultrathin hydrogel and its conformable attachment on a green leave. Besides esthetic purposes, high transmittance also allows direct visualization of any adverse effects such as irritation, allergy, and inflammation, which is especially beneficial for prolonged monitoring (*46*, *47*). The capability of large-scale fabrication with an area of 100 cm$^2$ is demonstrated in fig. S8. After freeze-drying the ultrathin hydrogel, SEM characterization illustrates highly porous structure of the ultrathin hydrogel, as shown in Fig. 2F. The WVTR of the ultrathin hydrogel was also
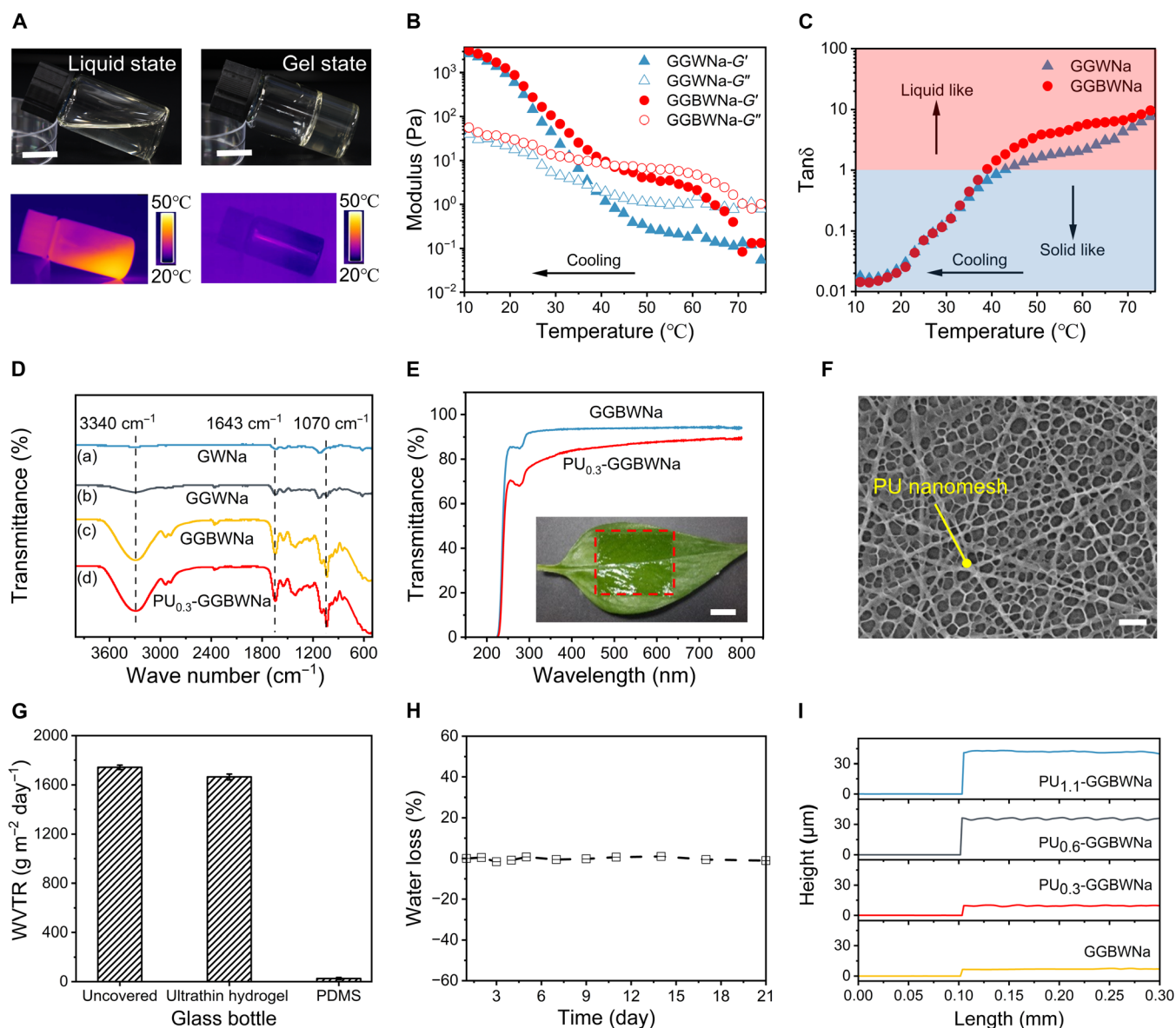
**Fig. 2. Characterization of thermally responsive phase change hydrogel materials and the ultrathin hydrogels.** (**A**) Photographs and infrared camera images of hydrogels at high temperature (55°C) and room temperature (25°C), illustrating their temperature-dependent phase change properties. Scale bar, 1 cm. (**B**) Rheological characterization of hydrogels solution with different recipes at a temperature sweep from 75° to 10°C, showing their transition between viscous liquid state and viscoelastic gel state. (**C**) The corresponding tanδ ($G''/G'$) calculated from (B). (**D**) FTIR spectra of hydrogels with different formulations and the ultrathin hydrogel. (**E**) Optical transmittance of the GGBWNa and PU$_{0.3}$-GGBWNa, the insert photograph demonstrating the ultrathin hydrogel conformably attached on a green leave. Scale bar, 1 cm. (**F**) SEM image of the internal structure of the freezing-dried ultrathin hydrogel. Scale bar, 5 μm. (**G**) Comparison of WVTR for an uncovered bottle, a bottle covered with 1000-μm-thick PDMS film, and a bottle covered with ~10-μm-thick ultrathin hydrogel, respectively. (**H**) Anti-drying performance of the ultrathin hydrogel for 21 days under ambient environment. (**I**) Thickness comparison of hydrogels and PU nanomesh–reinforced hydrogels. Error bars represent the SD of the measured values ($n = 3$).

experimentally investigated (Fig. 2G). The ultrathin hydrogel exhibits almost the same WVTR of 1669.3 ± 23.5 g m$^{-2}$ day$^{-1}$ as the open bottle (1742.8 ± 18.3 g m$^{-2}$ day$^{-1}$) due to the thinness geometry and porous structure. The reported value of human sweat evaporation rate is about 600 g m$^{-2}$ day$^{-1}$ (28); thus, the gas permeability of the ultrathin hydrogel is sufficient to allow gas diffusion from the skin underneath. It is worth noting that increasing hydrogel thickness would lead to lower WVTR (fig. S9). In addition to gas permeability and conformability, anti-drying capacity is also an important factor for long-term health monitoring. Because of the water-locking

capacities of glycerol in the ultrathin hydrogel, the water loss was maintained at nearly 1% over a 21-day storage under an ambient environment (Fig. 2H). In contrast, the glycerol-free ultrathin hydrogel dried out rapidly within 24 hours, where the water loss was up to 41.1% after a 2-day storage (fig. S10). It should be noted that the nanomesh densities influence the thickness of the reinforced hydrogels (42). To quantitatively investigate the effect of the PU nanomesh density on the thickness of hydrogels, we prepared four kinds of hydrogels with PU nanomesh densities of 0, 0.3, 0.6, and 1.1 mg cm$^{-2}$, referred to as GGBWNa, PU$_{0.3}$-GGBWNa (i.e., ultrathin hydrogel),

$PU_{0.6}$-GGBWNa, and $PU_{1.1}$-GGBWNa, respectively. As illustrated in Fig. 2I, the thickness of four samples was 6.7, 9.6, 35.9, and 40.2 μm, respectively, consistent with cross-sectional SEM images (fig. S11).

## Mechanical and adhesive characteristics of PU nanomesh–reinforced hydrogels

The concrete-like reinforced structure was proposed to overcome the trade-off effect between geometric thinness and the mechanical robustness of hydrogels (22, 42). During stretching, the nanomeshes become elongated owning to the stretchable mesh structure and the elastic hydrogel material; the elongated nanomeshes return to their original stage upon strain releasing (fig. S12) (21). Figure 3A exhibits that the tensile strength of PU nanomesh–reinforced hydrogel is significantly higher than that of pure PU nanomeshes and GGBWNa

hydrogels. The stretchability of $PU_{0.3}$-GGBWNa, $PU_{0.6}$-GGBWNa, and $PU_{1.1}$-GGBWNa reached $606 \pm 29.6\%$, $696 \pm 26.3\%$, and $646 \pm 11.9\%$ strain, respectively (fig. S13). As expected, higher nanomesh densities lead to hydrogels with higher Young's modulus and toughness (Fig. 3B) (42). The Young's modulus and toughness of $PU_{0.3}$-GGBWNa, $PU_{0.6}$-GGBWNa, and $PU_{1.1}$-GGBWNa increased from $4.4 \pm 0.8$ to $19.1 \pm 3.1$ kPa and $7.3 \pm 1.0$ to $44.8 \pm 7.8$ kJ m$^{-3}$, respectively. With the same nanomeshes density of 0.3 mg cm$^{-2}$, thicker hydrogels exhibit lower Young's modulus and toughness because of the lower content of nanomeshes (fig. S14) (42). Compared with previous work of gelatin-based EEG hydrogel sensors (19), we successfully prepared an ultrathin hydrogel with a 1000 times smaller thickness, however, with 1.2 times higher stretchability. The cyclic tensile experiment indicates that the ultrathin hydrogel could survive 1000 stretching and releasing cycles under 100% strain (Fig. 3C). There is a distinct hysteresis loop
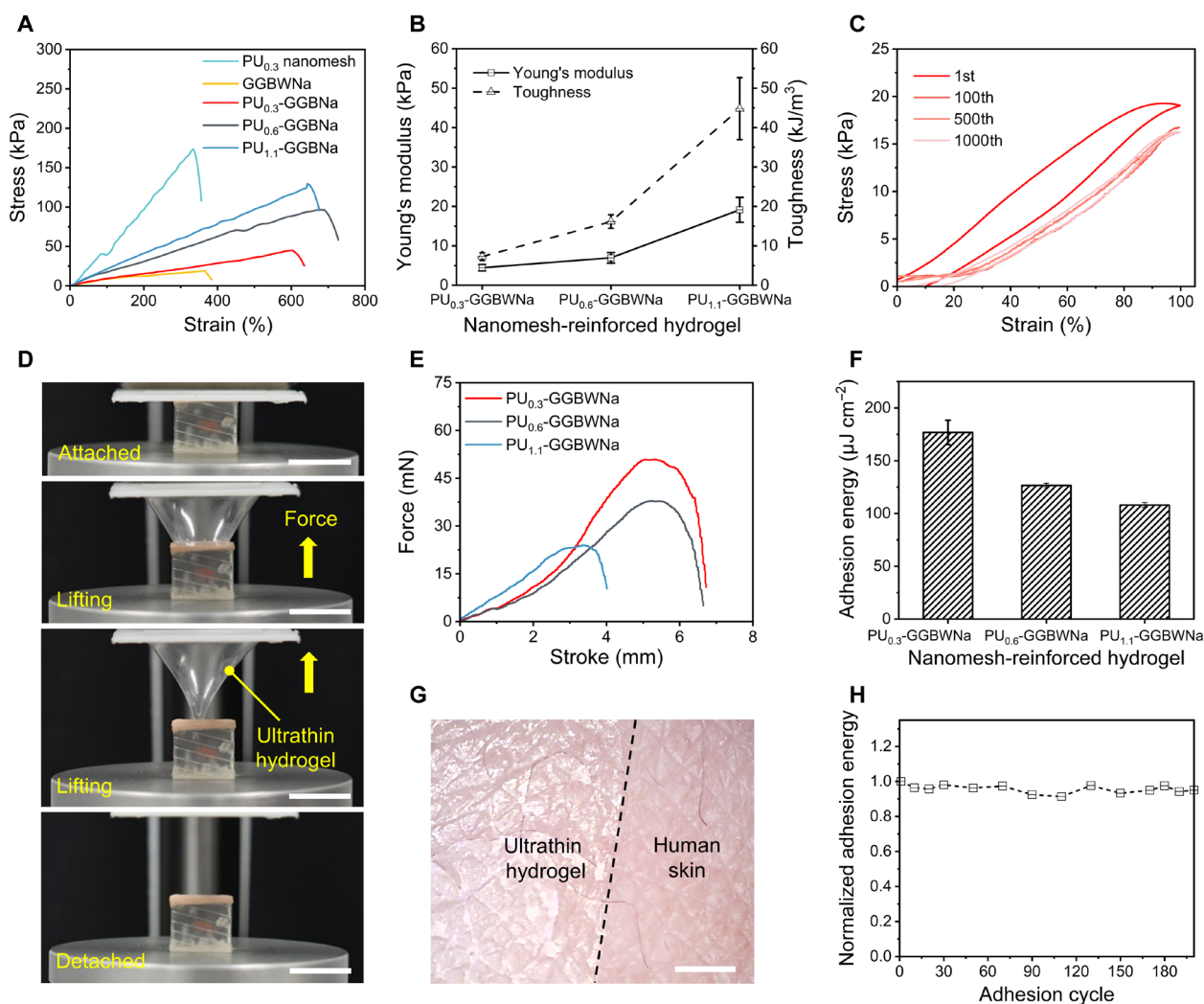


**Fig. 3. Mechanical and adhesive characteristics of the PU nanomesh–reinforced hydrogels.** (**A**) Tensile stress curves of PU nanomeshes, hydrogels, and PU nanomesh–reinforced hydrogels. (**B**) Comparison of Young's modulus and toughness of PU nanomesh–reinforced hydrogels calculated from (A). (**C**) Cyclic stretching/releasing curves of the ultrathin hydrogel under 100% strain. (**D**) Photographs demonstrating the separation process of the ultrathin hydrogel from artificial skin in a tack separation experiment. Scale bar, 1 cm. (**E**) Force stroke curves of PU nanomesh–reinforced hydrogels. (**F**) Comparison of the area adhesion energy and separation stroke for the PU nanomesh–reinforced hydrogels on artificial skin. (**G**) Microscope image of the ultrathin hydrogel seamlessly attached to the human skin. Scale bar, 1 cm. (**H**) Normalized adhesion energy of the ultrathin hydrogel during 200 attaching/detaching adhesion cycles. Error bars represent the SD of the measure values ($n = 3$).

in the first tensile loading/unloading cycle due to the energy dissipation in the viscoelastic hydrogels; the subsequent almost overlapped tensile stress curves demonstrated great fatigue resistance of the ultrathin hydrogels owing to the rapid dissociation and recovery of the physical interactions in the hydrogel matrix (48). Notably, the Young's modulus of the ultrathin hydrogel is lower than that of the human skin (0.1 to 2 MPa) (49, 50), enabling high conformability as skin sensors.

An effective approach to achieving low skin contact impedance is to reduce the interfacial gap between the human skin and the skin sensor by enhancing adhesion properties (15). There are two strategies for adhesion improvement: (i) decrease sensor thickness to obtain high skin compliance and (ii) construct chemical and/or physical bonds between the human skin and the sensor. Flexural rigidity indicates the capability of the compliance of a plate film to a three-dimensional surface, which is defined as $D = \frac{Et^3}{12(1-v^2)}$. Here, $E$, $t$, and $v$ represent Young's modulus, thickness, and Poisson's ratio of the film, respectively (42). Therefore, reducing the thickness is the most effective pathway to decrease flexural rigidity. Instead of the adhesion evaluation tests, such as ASTM F2256 for 180° peel test and ASTM F2255 for lap-shear test, which are widely used for tissue adhesives, a tack separation experiment was performed to investigate the adhesion properties in this work, as previously proposed to evaluate a 650-nm-thick polydopamine-modified polydimethylsiloxane (PDMS) nanosheet (51). In the experiment, we used an artificial skin as the target surface, the adhesion force was recorded by a universal tensile tester when the holder gradually lifted at a speed of 10 mm min$^{-1}$ until the ultrathin hydrogel was completely separated from the artificial skin (Fig. 3D and movie S4). Figure S15 statically demonstrated that reinforced hydrogels with lower thickness have a higher area adhesion energy owing to the significantly decreased flexural rigidity. Besides, the abundance of the amino acid groups, anions, and cations in the gelatin hydrogels facilitate strong and reversible bonding to various surfaces via chemical and physical bonds, such as hydrogen bonding, electrostatic interactions, and complexation bonding (Fig. 1E and fig. S16) (52). As evidenced in fig. S15, reinforced hydrogels have much higher area adhesion energy and separation stroke than reinforced PDMS films with the same thickness.

The adhesion results show that the ultrathin hydrogel exhibits an area adhesion energy of up to 176.8 μJ cm$^{-2}$ and an adhesion stroke of 6.7 mm (Fig. 3, E and F). Figure 3G demonstrates the ultraconformal and seamless skin contact of the ultrathin hydrogel, where the peeled-off ultrathin hydrogel presents distinct replicated microscopic skin texture (fig. S17). Besides, the ultrathin hydrogel moves along with natural skin motions during stretching and compressing without additional fixtures or adhesives owing to the ultralow Young's modulus and self-adhesiveness (fig. S18 and movie S5). In particular, good adhesion performance was maintained with area adhesion energy exceeding 90% after 200 attaching/detaching adhesion cycles, demonstrating a capability of repeated usage for health monitoring (Fig. 3H). To determine the appropriate adhesion force for a wearable device, we compared the adhesion performance of the ultrathin hydrogel and commercial baby-safe ECG gel. The results show that the area adhesion energy of the ultrathin hydrogel is 0.3 times lower than that of commercial baby-safe gels, however, with a 100 times smaller thickness (fig. S19). Therefore, the adhesion force of ultrathin hydrogels does not cause irritation to the human skin after detachment. All materials in this work, including gelatin, glycerol, borax, and Na$_2$SO$_4$, are nontoxic and biocompatible (19, 53). We took photos before, over, and after 24 hours of continuous wearing to observe any negative sensations or feelings on the human skin. The results show that there is no skin irritation, itches, or inflammation caused by continuous attachment or peeling off the ultrathin hydrogels (fig. S20).

## Long-term, continuous high-fidelity ECG monitoring by the ultrathin hydrogels under daily life conditions

To obtain long-term high-quality electrophysiological signals, one important criterion is to construct a stable and low-impedance interface between the electrodes and human skin (54). As shown in Fig. 4A, the skin-electrode impedance of the ultrathin hydrogels (31.3 kilohms, ~10 μm thick) was lower than that of commercial gels (57.5 kilohms, ~1 mm thick) at 100 Hz. Both were sufficiently low for bioelectrical signal recording (29). The low impedance of the ultrathin hydrogel is attributed to (i) high ionic conductivity of $9.3 \pm 0.5$ S/m (table S1) and (ii) minimized interfacial gap between the hydrogel and the human skin by the great self-adhesiveness of the hydrogel material (25). The impedance maintenance over 24 hours of continuous wearing is shown in fig. S21, where the profiles almost coincided with the initial curve, indicating the long-term skin applicability of the ultrathin hydrogels. We then adopted the ultrathin hydrogel for long-term, continuous wireless ECG monitoring (Fig. 4, B to F). Figure 4B illustrates the placement of ultrathin hydrogels for ECG monitoring, and a detailed measurement setup is presented in fig. S22. Two ultrathin hydrogels self-adhered on the chest of the subject and connected to a portable wireless module with Bluetooth component to collect ECG signal in real time. The characteristic waveforms were successfully captured with a high signal-to-noise ratio (SNR) of $32.8 \pm 1.6$ dB by the ultrathin hydrogels, while commercial gels showed similar waveforms but smaller SNR of $29.7 \pm 1.0$ dB (Fig. 4C). Furthermore, the resting heart rate detected by ultrathin hydrogels was consistent with the commercial photoplethysmogram ring, validating its accuracy (fig. S23). To evaluate sweat influence, we conducted an experiment to examine the electrode capability of ECG monitoring during workout-induced sweating. The results show distinguishable informative ECG waveforms with an SNR of $31.1 \pm 2.2$ dB after 20 min of strenuous exercise, indicating that sweating has a negligible effect on ECG monitoring (fig. S24). The main reason may be (i) the excellent gas/vapor permeability of the ultrathin hydrogel and (ii) reduced skin contact impedance induced by the slightly increased temperature and ionic conductivity by sweat (19). Considering the hydrophilicity of gelatin hydrogel, the long-term stability under sweat conditions requires further systematic investigation.

Figure 4 (D and F, top) exhibits continuous ECG signals while the subject was performing various normal daily activities [e.g., personal computer (PC) work, walking, sleeping, doing laboratory experiments, and eating] on day 1 from 11:00 a.m. to 11:00 p.m. and day 8 from 2:00 p.m. to 2:00 a.m., respectively. The zoomed-in segments in Fig. 4 (D and F) showed pronounced ECG waveforms. The differences in amplitude were caused by moving away from the receiver or varied sleep stages of the subject (Fig. 4, D and F). We further analyzed the average heart rate during different activities, such as PC working [73.7 beats per minute (bpm)], working (64.6 bpm), sleeping (59.8 bpm), and performing a laboratory experiment (75.3 bpm) on day 1 and PC working (67.3 and 70.3 bpm) and eating dinner (72.5 bpm) on day 8, respectively (Fig. 4, D and F, bottom). ECG signals recorded from day 2 to day 7 also exhibited stable and characteristic peaks (Fig. 4E). The SNR remained almost the same during the whole measurement procedure, with an average value of up to $32.2 \pm 1.3$ dB (fig. S25). The ultrathin hydrogel successfully
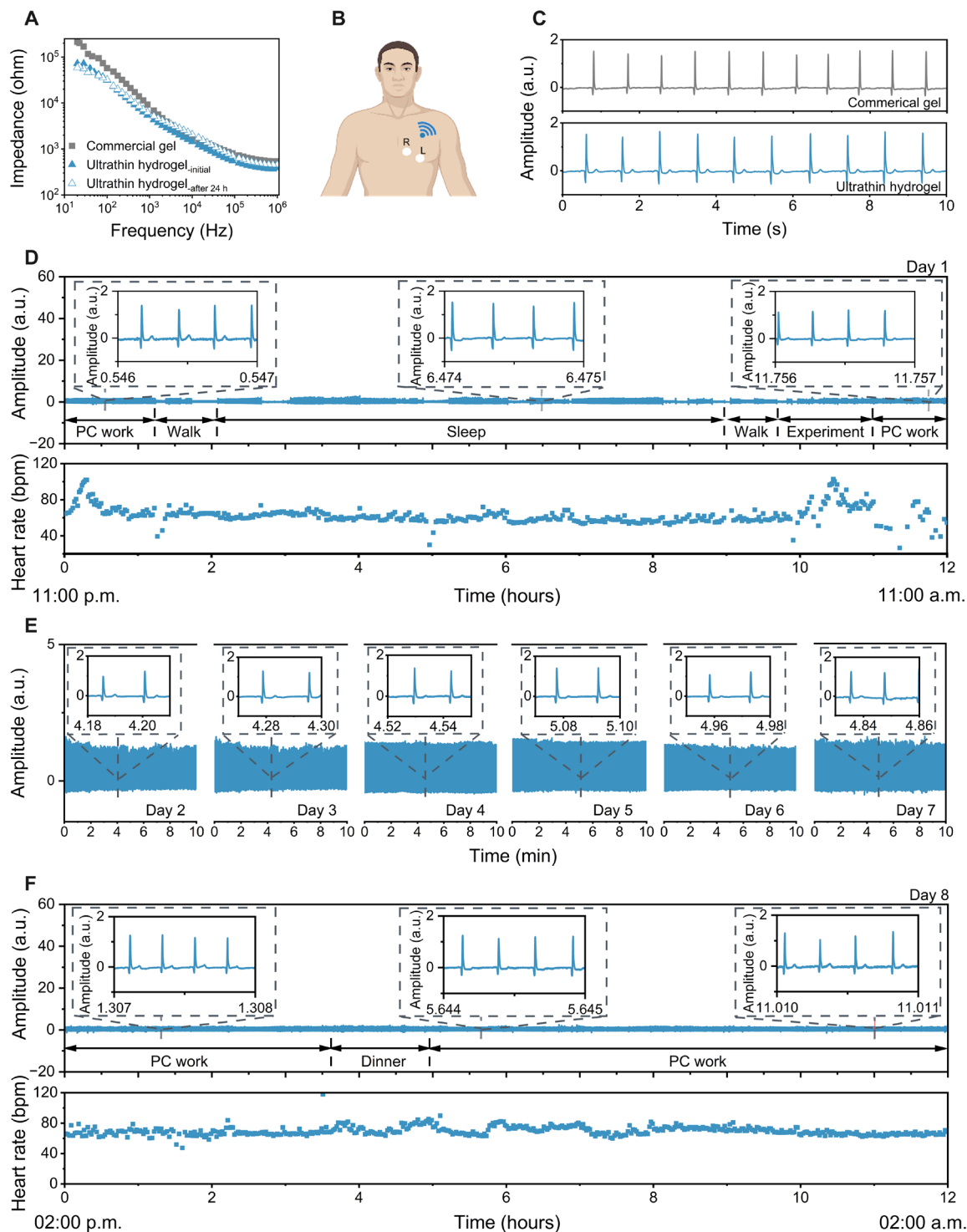
**Fig. 4. Long-term, continuous high-fidelity ECG monitoring by the ultrathin hydrogels under daily life conditions.** (**A**) Skin-electrode contact impedance analysis of commercial gels and ultrathin hydrogels. (**B**) Schematic illustration of the experimental setup for wireless ECG measurement. (**C**) ECG signals recorded by commercial gels (top) and ultrathin hydrogels (bottom) in a sedentary state. (**D**) ECG signals monitoring (top) and the heart rate results (bottom) by the ultrathin hydrogels during various normal daily activities on day 1 from 11:00 a.m. to 11:00 p.m. The insets show the zoomed-in data segments. (**E**) ECG signals monitoring from day 2 to day 7, the insets show the zoomed-in data segments. (**F**) ECG signals monitoring (top) and the heart rate results (bottom) by the ultrathin hydrogels during various normal daily activities on day 8 from 2:00 p.m. to 2:00 a.m., respectively. a.u., arbitrary units; PC, personal computer.

demonstrates 8-day continuous high-fidelity ECG monitoring under daily life conditions, attributing to the combined properties of thinness geometry, high gas permeability, outstanding mechanical robustness, great dynamic skin conformability, and long-term anti-drying capacity. We performed an 8-day continuous wearing and monitoring as the battery of the wireless module ran out of power after 8 days. To fully demonstrate the behavior of electrodes over time, we did further experiments on wireless ECG monitoring over a 12-day continuous wearing. The results show that the skin contact impedance (at 100 Hz) exhibits a slight change from 36.6 kilohms on day 5 to 52.4 kilohms on day 12, mainly contributed by the changes in body temperature and sweat conditions (fig. S26, A and B). These changes had minimum effect on the ECG signal quality (fig. S26C). The ultrathin hydrogel is able to collect high-fidelity ECG signals with an SNR of $29.8 \pm 2.0$ dB after 1 to 21 days of storage under ambient environment (fig. S27). The above results suggest great potentiality of the ultrathin hydrogels for early diagnosis of cardiac disorders, such as bundle branch block and Brugada syndrome (55).

### Other long-term high-fidelity electrophysiological monitoring by the ultrathin hydrogels

We further exploited other electrophysiological monitoring, such as EMG, MCV, EOG, EEG, ABR, and VEP, using the ultrathin hydrogels. For EMG monitoring, two ultrathin hydrogels were placed on the brachioradialis muscles, and commercial gels were used as control samples (fig. S28A). The signals collected by ultrathin hydrogels present similar waveforms with an SNR of 38.2 dB to the commercial gels with an SNR of 38.4 dB when the subject was making a fist (fig. S28B). High-quality EMG signals with an average SNR of 37.8 dB were obtained by the ultrathin hydrogels after 24 hours of continuous wearing. For MCV signals, electric current is usually used to stimulate the muscles and nerves of the human body, which can diagnose whether the peripheral motor nerves are in good condition (56). As presented in Fig. 5A and movie S6, two ultrathin hydrogels were placed on the thenar cavity to capture MCV signals by stimulating the peripheral nerves. Figure 5B shows that both ultrathin hydrogels and commercial gels exhibit bidirectional high-amplitude waveforms, which are typically "M"-shaped. The duration of the acquired signals from the ultrathin hydrogels (0.7 ms) was comparable to that of the commercial gels (0.7 ms). While the amplitude of the acquired signals from the ultrathin hydrogels (8.7) was higher than that of the commercial gels (7.4). Figure 5C displays the application of ultrathin hydrogels in EOG monitoring. The representative periodic EOG signals recorded by the ultrathin hydrogels and commercial gels can be intuitively seen when the subject constantly moves his eyes from side to side (Fig. 5D).

High-quality and noninvasive recording of EEG signals are difficult to collect due to the weak signals in microvolt range and interference of dense hairs. We placed two ultrathin hydrogels on the forehead according to the 10 to 20 international EEG system (Fig. 5E). The EEG signals acquired by the ultrathin hydrogels show negligible differences in terms of signal amplitude and power spectral density, even after 24-hour wearing (Fig. 5, F and G). Evoked potentials are important for neurological disease diagnosis, especially for patients who cannot complete the inspection autonomously (57). Figure 5H illustrates the painted hydrogels on the central of the head and two ears as reference electrodes for ABR signal monitoring. The ABR waveforms were generated by stimulating the ear with a sound of a certain intensity. The characteristic waveforms (I, II, III, IV, and V)

were successfully captured within 10 ms by auditory stimulation, which means the auditory function of the subject was normal (Fig. 5I). Otherwise, it indicates that the auditory function of the subject was impaired. The signal profiles by the ultrathin hydrogels were also maintained after 24 hours of continuous wearing. Given that the human eyes are sensitive to contrast changes such as pattern flip stimuli, we stimulated the left eye to capture the VEP waveforms by the black and white grid flicker (Fig. 5J). Figure 5K depicts that the characteristic P100 waveforms appeared for both hydrogels and commercial gels within a normal range of 89 to 114 ms, here P100 represents the transient potential of VEP with a latency of about 100 ms (58). Furthermore, the developed hydrogels demonstrated capabilities of high-quality VEP monitoring after 24-hour continuous skin wear. Last, the ultrathin hydrogels also successfully demonstrated the capability of a durable on-skin strain gauge (fig. S29). For on-skin applications, the temperature-dependent phase transition characteristic of the hydrogel materials can be used to easily remove the hydrogel from the hairy skin by using a hair dryer (fig. S30).

## DISCUSSION

Compared with our previous work, where a gelatin-based temperature-controlled phase change paintable biogel was developed for intermittent health monitoring for 3 days (19), the present ultrathin, gas-permeable hydrogels can realize continuous health monitoring for 8 days under daily life conditions. In summary, the conductive hydrogel skin sensors evolve from bulky and fragile form factors with limited gas permeability to robust thinness geometry with excellent gas permeability by taking advantage of the reversible thermal-responsive phase change features and nanofiber reinforcement strategy. Nonetheless, to enable adaptability to extreme conditions, such as extreme temperature, humidity, mechanical damage, and acidic/alkaline environments, advanced materials development is required to concurrently obtain corresponding adaptable properties for long-term, continuous skin applicability. Besides, it is also necessary to integrate artificial intelligence for high-precision diagnosis and therapy in digital health as well as precision control in human/brain-machine interfaces. This work provides promising material and engineering solutions for the development of hydrogel-enabled skin bioelectronics for long-term applications and represents an important step toward noninvasive personalized health care.

## MATERIALS AND METHODS
### Materials

Type A gelatin powder from porcine skin with a Bloom number of ~300 g was purchased from Sigma-Aldrich. Glycerol, sodium tetraborate decahydrate (i.e., borax), sodium sulfate anhydrous, N,N-dimethylformamide, and tetrahydrofuran were purchased from Aladdin Industrial Corporation. PU (1185A) was obtained from Badische Anilin- und Soda-Fabrik Polyurethanes (BASF) GmbH. All reagents used in this work were of analytical grade and were used without further purification. The commercial ECG gels (~1 mm thick) and baby-safe ECG gels (~1 mm thick) were purchased from (Vitrode L, NIHON KOHDEN, Japan) and (Suzhou Letai Medical Technology Co. Ltd., China), respectively.

### Preparation of ultrathin yet mechanically robust hydrogels

The ultrathin hydrogel was designed by dip-coating PU nanomeshes into a hydrogel solution with thermal-controlled phase transition
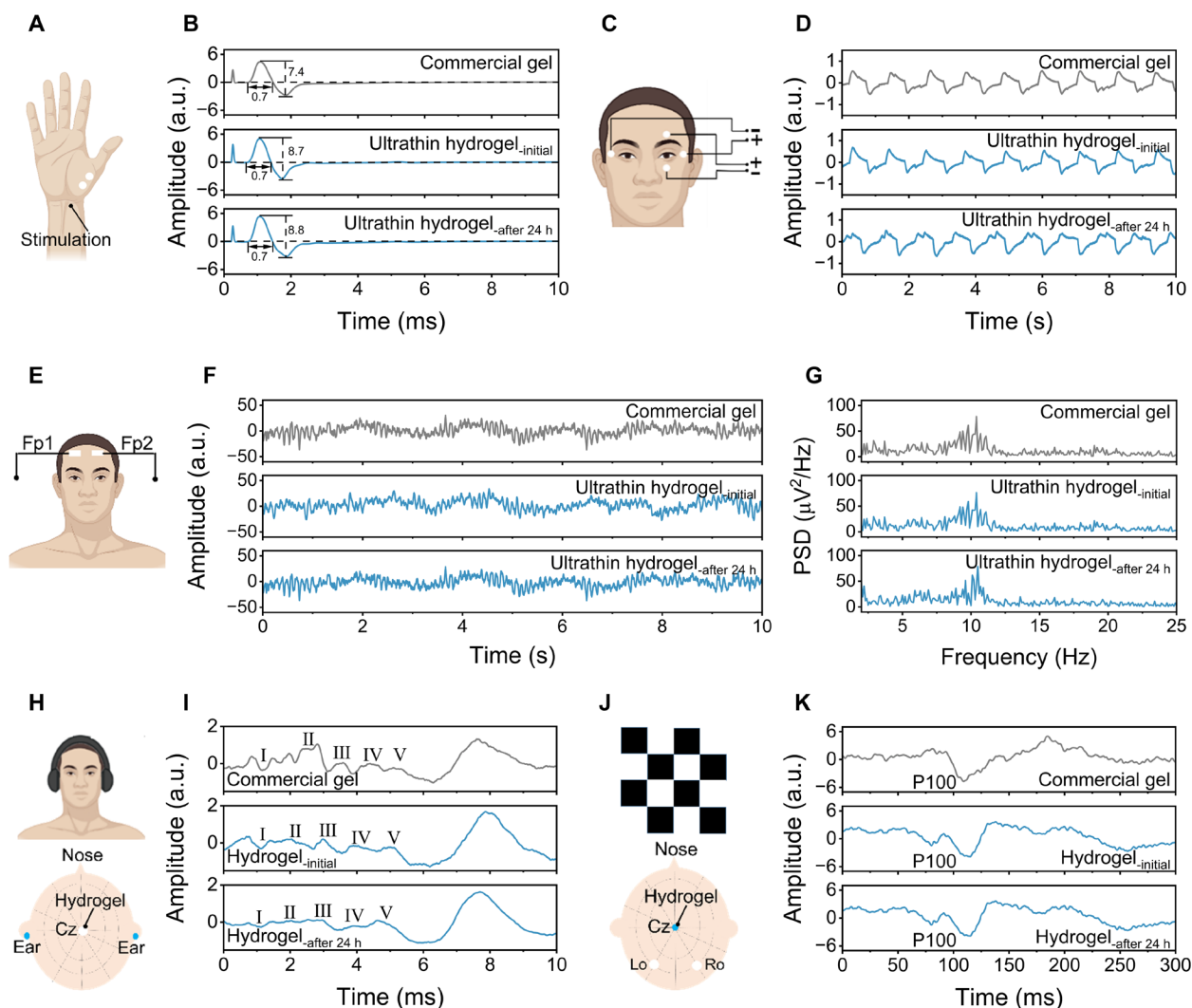
**Fig. 5. Other long-term high-fidelity electrophysiological monitoring by the ultrathin hydrogels.** (**A**) Schematic illustration of the experimental setup for measuring MCV signals. (**B**) MCV signals recorded by commercial gels and ultrathin hydrogels. (**C**) Schematic illustration of the experimental setup for measuring EOG signals. (**D**) EOG signals recorded by commercial gels and ultrathin hydrogels. (**E**) Schematic illustration of the experimental setup for measuring EEG signals. (**F**) EEG alpha rhythms recorded by commercial gels and ultrathin hydrogels. (**G**) The power spectral density of EEG signals obtained from (F). (**H**) Schematic illustration of the experimental setup for measuring ABR signals. (**I**) ABR waveforms recorded by commercial gels and hydrogels. (**J**) Schematic illustration of the experimental setup for measuring VEP signals. (**K**) VEP signals recorded by commercial gels and hydrogels. All mentioned physiological markers were monitored throughout 24 hours of continuous wearing. a.u., arbitrary units.

features and then gelating at a physiological temperature or under ambient environment. PU nanomeshes were fabricated by a previously reported electrospinning method (*59*). One gram of PU was dissolved in a 6.7 g of mixed solvent (*N*, *N*-dimethylformamide and tetrahydrofuran with a mass ratio of 1:1) and stirred for 12 hours at 25°C in a dark environment to obtain a 13 wt % PU solution. Subsequently, the as-prepared solution was loaded in a 5-ml syringe with a 27-gauge-diameter metallic needle and placed in the electrospinning apparatus (YFSP-T, Tianjin Yunfan, China) at a voltage of 11 kV and a flow rate of 0.001 mm s$^{-1}$. The distance between the metallic needle and the collector was 12.5 cm, and the PU nanomeshes were collected on a rotating drum covered with silicone-coated paper. The suspended PU nanomeshes could be obtained by transferring PU nanomeshes onto a polyimide frame with desired size. The

thermal-controlled phase transition hydrogel solution was synthesized via a one-pot method. A total of 2.5 g of gelatin was dissolved in a water/glycerol (with a mass ratio of 2:7) binary system, followed by adding 1.5 g of borax and 1.3 g of Na$_2$SO$_4$. The mixture was stirred for 2 hours at 55°C to form a homogeneous hydrogel solution. To regulate the temperature of the thermal-dependent hydrogel, a heated magnetic stirrer (C-MAG HS 7 control, IKA-Werke GmbH & Co. KG, Germany) was used to conduct this experiment. The detailed formulas are shown in table S2.

## Characterization of ultrathin hydrogels
FTIR spectra were obtained using an FTIR spectrometer (Nicolet iS50, Thermo Fisher Scientific, USA) in the frequency range of 4000 to 400 cm$^{-1}$ with a total of 32 scans and a resolution of 4 cm$^{-1}$. The surface and

cross-sectional morphology of ultrathin hydrogels were acquired using a SEM instrument (TM4000, HITACHI, Japan) at a voltage of 15 kV. For cross-sectional SEM characterization, the ultrathin hydrogel was attached to an anodisc substrate and embrittled in liquid nitrogen. For surface SEM measurement, the ultrathin hydrogel was rinsed in deionized water before freeze-drying to remove glycerol residues. The optical microscopic images were acquired using a mobile digital microscope instrument (AM7515MT8A, Dino-Lite, Japan). The rheological properties were characterized by a rheometer (HR-1, TA instruments, USA) with a dynamic temperature sweep mode from 75° to 10°C and from 10° to 75°C at a rate of 2°C min$^{-1}$, and the oscillation frequency was $2\pi$ rad s$^{-1}$ at a shear strain of 1%.

## Mechanical and tack separation test

The mechanical properties were measured using a universal tensile tester (ESM303, Mark-10, USA) with a 10 N load cell. All samples were transferred to a 15 mm–by–8 mm suspended polyimide frame and placed vertically on a tensile tester. Then, separated the sample from the left and right sides of the polyimide frame, followed by cutting off the left and right sides of the polyimide frame with a sharp knife for tensile testing. All samples were stretched at a rate of 10 mm min$^{-1}$. For tack separation measurement, the ultrathin hydrogel was placed on a 3D-printed holder with a size of 2 cm by 2 cm. The initial contact area between the ultrathin hydrogel and artificial skin was 1 cm by 1 cm. The adhesion force was recorded by the universal tensile tester when the holder gradually lifted at a speed of 10 mm min$^{-1}$ until the ultrathin hydrogel was completely separated from the artificial skin. The adhesion energy can be calculated by the following equation (42)

$$E = \int_{0}^{x} y dL \tag{1}$$

where $E$, $x$, $y$, and $L$ are adhesion energy, separation stroke, separation forces, and stroke, respectively.

## Evaluation of WVTR and anti-drying property

Ten grams of deionized water in glass bottles with an open diameter of 12 mm was weighted. Glass bottles with different coverings were placed in a thermostatic chamber at 25°C with a humidity of 30%. Weight loss of each bottle was measured after 24 hours. The WVTR can be obtained by the following equation (60)

$$WVTR = \frac{m_{loss}}{t \times S} \tag{2}$$

where $m_{loss}$, $t$, and $S$ are the water loss weight, time, and surface area, respectively.

To measure the anti-drying capability, the ultrathin hydrogel was placed in an ambient environment for 21 days. The anti-drying ability was obtained by the following equation

$$Water\ retention\ (\%) = \frac{m_t}{m_0} \times 100 \tag{3}$$

where $m_0$ and $m_t$ are the weight of the ultrathin hydrogel at day 0 and day $t$, respectively.

## Measurement of impedance and electro-mechanical properties of ultrathin hydrogel-based sensors

An inductance-capacitance-resistance meter (LCR) meter (E4980AL, Keysight, USA) with frequencies ranging from 1 MHz to 20 Hz was used to measure the intrinsic impedance of ultrathin hydrogels with different glycerol and Na$_2$SO$_4$ content. The ultrathin hydrogel (1 cm by 2 cm) was placed on an interdigitalized electrode. To measure the skin-electrode contact impedance, ultrathin hydrogels with 3.0 cm–by–3.5 cm size were integrated with flexible Ag/AgCl electrodes, and commercial ECG electrodes were used with the same size as a comparison. The distance between the two electrodes' edges was ~2 cm. For electromechanical characterizations, a motorized moving stage (LTS150/M, Thorlabs, USA) was used to stretch the samples. Simultaneously, the LCR meter was used to record the resistance. Note that all samples were in the same size of 1.5 cm by 1 cm.

## Electrophysiological recording

For wireless ECG monitoring, two ultrathin hydrogels with a circular shape (diameter of 2 cm) integrated with metal ECG snap buttons were attached to the left chest of the subject and connected to a commercial wireless module (GM3 Co. Ltd., Japan). Detailed sensor placement is shown in Fig. 4B, and R and L denote the spot of the right electrode and left electrode, respectively. The experimental setup can be seen in fig. S20. For the 21-day ECG signal recording, two ultrathin hydrogels with flexible Ag/AgCl electrodes as recording electrodes were placed on the left and right sides of the chest, respectively. The electrodes were connected to a signal recording system (MEB-2312C, NIHON KOHDEN, Japan) with a bandpass filter (0.02 to 50 Hz). In this experiment, the subject wore the ultrathin hydrogels for ~10 min daily during measurement.

For EMG signal recording, two ultrathin hydrogels with flexible Ag/AgCl electrodes were adhered to the brachioradialis muscles as reference electrodes, and another ultrathin hydrogel was attached on the hand dorsum as a ground electrode (fig. S28A). All electrodes were connected to the signal recording system with a bandpass filter (10 Hz to 10 kHz). The EMG signals were generated when the subject opened and clenched fist. The MCV signal was monitored by placing two ultrathin hydrogels on the thenar cavity as reference electrodes and commercial gels in adjacent locations for simultaneous measurements (Fig. 5A). The electrodes were connected to the signal recording system with a bandpass filter (10 Hz to 5 kHz), and the signals were recorded by stimulating the peripheral nerve. The stimuli intensity was 5.4 mA at a stimuli frequency of 4.7 Hz.

A dual-channel lead was used for EOG signal recording; one ultrathin hydrogel with flexible Ag/AgCl electrode was placed above the subject's eyebrows, and one on the lower orbital edge. The two hydrogels were in line with the eyeball. Two additional ultrathin hydrogels were placed on the outer of the left and right orbits, and another electrode was attached to the center of the forehead as a ground electrode (Fig. 5C). All electrodes were connected to the signal recording system with a bandpass filter (1 to 200 Hz), and the signals were generated when the subject constantly moved his eyeballs from side to side.

A healthy male volunteer participated in the EEG recording. Two ultrathin hydrogels with flexible Ag/AgCl electrodes were placed on the cleaned forehead (Fp1 and Fp2) and commercial EEG paste was painted on the ear as ground electrode according to the 10 to 20 international electrode placement system. Detailed sensor placement is shown in Fig. 5E. For comparison, two commercial gels were simultaneously placed adjacent to the ultrathin hydrogel. All electrodes were connected to the signal recording system with a bandpass filter (0.05 to 50 Hz) for recording and processing. The EEG signals were generated when the subject closed his eyes in a sedentary state.

For ABR monitoring, a hydrogel electrode was painted on the central of the head (Cz) as recording electrode and another two on the ears as reference electrodes (Fig. 5H). The commercial gels were painted at the adjacent position for comparison. The electrodes were connected to the signal recording system with a bandpass filter (100 Hz to 3 kHz), and an earphone was used as the auditory stimulator. The ABR waveforms were generated by stimulating the left ear with 80-dB clicking sound and the right ear with 50-dB masking noise, superimposing 1000 times at a stimulating frequency of 10 Hz. In VEP recording, three hydrogel electrodes were painted on the left (Lo) and right occipital (Ro) position and Cz of the head, and two more hydrogel electrodes were pasted on the ears as reference electrodes (Fig. 5J). In comparison, the commercial gels were placed adjacent to the hydrogels. Then, all electrodes were connected to the signal recording system with a bandpass filter ranging from 100 Hz to 3 kHz for recording and processing. The waveforms are generated by stimulating the left eye with a black-and-white grid flicker at a frequency of 1 Hz. All experiments of physiological signals were thoroughly reviewed and approved by the internal ethical committee (approval no. E202204150001), and informed consent was obtained from subjects participating in the experiment.

## Supplementary Materials

**This PDF file includes:**
Figs. S1 to S30
Tables S1 and S2
Legends for movies S1 to S6

**Other Supplementary Material for this manuscript includes the following:**
Movies S1 to S6

## REFERENCES AND NOTES

1. Y. Haick, H. Sguo, C. Wang, S. Lee, T. Yokota, T. Someya, Skin bioelectronics towards long-term, continuous health monitoring. *Chem. Soc. Rev.* **51**, 3759–3793 (2022).
2. D.-H. Kim, N. Lu, R. Ma, Y.-S. Kim, R.-H. Kim, S. Wang, J. Wu, S. M. Won, H. Tao, A. Islam, K. J. Yu, T.-i. Kim, R. Chowdhury, M. Ying, L. Xu, M. Li, H.-J. Chung, H. Keum, M. McCormick, P. Liu, Y.-W. Zhang, F. G. Omenetto, Y. Huang, T. Coleman, J. A. Rogers, Epidermal electronics. *Science* **333**, 838–843 (2011).
3. M. L. Hammock, A. Chortos, B. C.-K. Tee, J. B.-H. Tok, Z. Bao, 25th anniversary article: The evolution of electronic skin (e-skin): A brief history, design considerations, and recent progress. *Adv. Mater.* **25**, 5997–6038 (2013).
4. K. Sagdic, E. Fernandez-Lavado, M. Mariello, O. Akouissi, S. P. Lacour, Hydrogels and conductive hydrogels for implantable bioelectronics. *MRS Bull.* **48**, 495–505 (2023).
5. Y. Ohm, C. Pan, M. J. Ford, X. Huang, J. Liao, C. Majidi, An electrically conductive silver-polyacrylamide-alginate hydrogel composite for soft electronics. *Nat. Electron.* **4**, 185–192 (2021).
6. C. Lim, Y. J. Hong, J. Jung, Y. Shin, S. H. Sunwoo, S. Baik, O. K. Park, S. H. Choi, T. Hyeon, J. H. Kim, S. Lee, D. H. Kim, Tissue-like skin-device interface for wearable bioelectronics by using ultrasoft, mass-permeable, and low-impedance hydrogels. *Sci. Adv.* **7**, eabd3716 (2021).
7. H. Yuk, B. Lu, X. Zhao, Hydrogel bioelectronics. *Chem. Soc. Rev.* **48**, 1642–1667 (2019).
8. J. Y. Sun, C. Keplinger, G. M. Whitesides, Z. Suo, Ionic skin. *Adv. Mater.* **26**, 7608–7614 (2014).
9. P. Zhou, Z. Zhang, F. Mo, Y. Wang, A review of functional hydrogels for flexible chemical sensors. *Adv. Sens. Res.* **2300021**, (2023).
10. H. Yuk, J. Wu, X. Zhao, Hydrogel interfaces for merging humans and machines. *Nat. Rev. Mater.* **7**, 935–952 (2022).
11. N. Tang, R. Zhang, Y. Zheng, J. Wang, M. Khatib, X. Jiang, C. Zhou, R. Omar, W. Saliba, W. Wu, H. Haick, Highly efficient self-healing multifunctional dressing with antibacterial activity for sutureless wound closure and infected wound monitoring. *Adv. Mater.* **34**, 2106842 (2021).
12. H. Kim, H. Lee, K.-Y. Seong, E. Lee, S. Y. Yang, J. Yoon, Visible light-triggered on-demand drug release from hybrid hydrogels and its application in transdermal patches. *Adv. Healthc. Mater.* **4**, 2071–2077 (2015).
13. Z. Zhang, Z. Zhu, P. Zhou, Y. Zou, J. Yang, H. Haick, Y. Wang, Soft bioelectronics for therapeutics. *ACS Nano* **17**, 17634–17667 (2023).
14. Z. Wu, X. Yang, J. Wu, Conductive hydrogel-and organohydrogel-based stretchable sensors. *ACS Appl. Mater. Interfaces* **13**, 2128–2144 (2021).
15. X. J. Sui, H. S. Guo, C. C. Cai, Q. S. Li, C. Y. Wen, X. Y. Zhang, X. D. Wang, J. Yang, L. Zhang, Ionic conductive hydrogels with long-lasting antifreezing, water retention and self-regeneration abilities. *Chem. Eng. J.* **419**, 129478 (2021).
16. M. Hua, S. Wu, Y. Ma, Y. Zhao, Z. Chen, I. Frenkel, J. Strzalka, H. Zhou, X. Zhu, X. He, Strong tough hydrogels via the synergy of freeze-casting and salting out. *Nature* **590**, 594–599 (2021).
17. S. Li, H. Pan, Y. Wang, J. Sun, Polyelectrolyte complex-based self-healing, fatigue-resistant and anti-freezing hydrogels as highly sensitive ionic skins. *J. Mater. Chem. A* **8**, 3667–3675 (2020).
18. Q. Ding, Z. Wu, K. Tao, Y. Wei, W. Wang, B.-R. Yang, X. Xie, J. Wu, Environment tolerant, adaptable and stretchable organohydrogels: Preparation, optimization, and applications. *Mater. Horiz.* **9**, 1356–1386 (2022).
19. C. Wang, H. Wang, B. Wang, H. Miyata, Y. Wang, M. O. G. Nayeem, J. J. Kim, S. Lee, T. Yokota, H. Onodera, T. Someya, On-skin paintable biogel for long-term high-fidelity electroencephalogram recording. *Sci. Adv.* **8**, eabo1396 (2022).
20. G. Ge, Y. Lu, X. Qu, W. Zhao, Y. Ren, W. Wang, Q. Wang, W. Huang, X. Dong, Muscle-inspired self-healing hydrogels for strain and temperature sensor. *ACS Nano* **14**, 218–228 (2020).
21. J. Wang, B. Wu, P. Wei, S. Sun, P. Wu, Fatigue-free artificial ionic skin toughened by self-healable elastic nanomesh. *Nat. Commun.* **13**, 4411 (2022).
22. Q. Gao, F. Sun, Y. Li, L. Li, M. Liu, S. Wang, Y. Wang, T. Li, L. Liu, S. Feng, Biological tissue-inspired ultrasoft, ultrathin, and mechanically enhanced microfiber composite hydrogel for flexible bioelectronics. *Nano-Micro Lett.* **15**, 139 (2023).
23. Q. Huang, Z. Zheng, Pathway to developing permeable electronics. *ACS Nano* **16**, 15537–15544 (2022).
24. W. Niu, Q. Tian, Z. Liu, X. Liu, Solvent-free and skin-like supramolecular ion-conductive elastomers with versatile processability for multifunctional ionic tattoos and on-skin bioelectronics. *Adv. Mater.* **35**, e2304157 (2023).
25. L. Pan, P. Cai, L. Mei, Y. Cheng, Y. Zeng, M. Wang, T. Wang, Y. Jiang, B. Ji, D. Li, A compliant ionic adhesive electrode with ultralow bioelectronic impedance. *Adv. Mater.* **32**, e2003723 (2020).
26. S. Li, Y. Cong, J. Fu, Tissue adhesive hydrogel bioelectronics. *J. Mater. Chem. B* **9**, 4423–4443 (2021).
27. H. Xue, D. Wang, M. Jin, H. Gao, X. Wang, L. Xia, D. a. Li, K. Sun, H. Wang, X. Dong, Hydrogel electrodes with conductive and substrate-adhesive layers for noninvasive long-term EEG acquisition. *Microsyst. Nanoeng.* **9**, 79 (2023).
28. Z. Ma, Q. Huang, Q. Xu, Q. Zhuang, X. Zhao, Y. Yang, H. Qiu, Z. Yang, C. Wang, Y. Chai, Permeable superelastic liquid-metal fibre mat enables biocompatible and monolithic stretchable electronics. *Nat. Mater.* **20**, 859–868 (2021).
29. A. Miyamoto, S. Lee, N. F. Cooray, S. Lee, M. Mori, N. Matsuhisa, H. Jin, L. Yoda, T. Yokota, A. Itoh, Inflammation-free, gas-permeable, lightweight, stretchable on-skin electronics with nanomeshes. *Nat. Nanotechnol.* **12**, 907–913 (2017).
30. S. Cheng, Z. Lou, L. Zhang, H. Guo, Z. Wang, C. Guo, K. Fukuda, S. Ma, G. Wang, T. Someya, Ultrathin hydrogel films toward breathable skin-integrated electronics. *Adv. Mater.* **35**, e2206793 (2023).
31. S. Lee, S. Franklin, F. A. Hassani, T. Yokota, M. O. G. Nayeem, Y. Wang, R. Leib, G. Cheng, D. W. Franklin, T. Someya, Nanomesh pressure sensor for monitoring finger manipulation without sensory interference. *Science* **370**, 966–970 (2020).
32. Y. Wang, S. Lee, T. Yokota, H. Wang, Z. Jiang, J. Wang, M. Koizumi, T. Someya, A durable nanomesh on-skin strain gauge for natural skin motion monitoring with minimum mechanical constraints. *Sci. Adv.* **6**, eabb7043 (2020).
33. C. H. Yang, Z. G. Suo, Hydrogel ionotronics. *Nat. Rev. Mater.* **3**, 125–142 (2018).
34. Y. Zhang, T. H. Tao, Skin-friendly electronics for acquiring human physiological signatures. *Adv. Mater.* **31**, e1905767 (2019).
35. X. C. Liu, Z. P. Huang, C. Q. Ye, Z. W. Luo, C. Chen, X. Y. Yao, F. Liang, T. Yang, H. C. Bi, C. L. Wang, C. H. Cai, L. J. Lyu, X. Wu, Graphene-based hydrogel strain sensors with excellent breathability for motion detection and communication. *Macromol. Mater. Eng.* **307**, 2200001 (2022).
36. S. Wei, R. Yin, T. Tang, Y. Wu, Y. Liu, P. Wang, K. Wang, M. Mei, R. Zou, X. Duan, Gas-permeable, irritation-free, transparent hydrogel contact lens devices with metal-coated nanofiber mesh for eye interfacing. *ACS Nano* **13**, 7920–7929 (2019).
37. L. You, X. Shi, J. Cheng, J. Yang, C. Xiong, Z. Ding, Z. Zheng, S. Wang, J. Wang, Flexible porous gelatin/polypyrrole/reduction graphene oxide organohydrogel for wearable electronics. *J. Colloid Interface Sci.* **625**, 197–209 (2022).
38. W. Liu, R. J. Xie, J. Y. Zhu, J. S. Wu, J. F. Hui, X. Y. Zheng, F. W. Huo, D. D. Fan, Advances in flexible organic field-effect transistors and their applications for flexible electronics. *npj Flexible Electron.* **6**, 1–10 (2022).
39. J. Cheng, L. You, X. Cai, J. Yang, H. Chen, X. Shi, J. Wu, J. Wang, C. Xiong, S. Wang, Fermentation-inspired gelatin hydrogels with a controllable supermacroporous structure and high ductility for wearable flexible sensors. *ACS Appl. Mater. Interfaces* **14**, 26338–26349 (2022).

40. M. Wu, X. Wang, Y. F. Xia, Y. Zhu, S. L. Zhu, C. Y. Jia, W. Y. Guo, Q. Q. Li, Z. G. Yan, Stretchable freezing-tolerant triboelectric nanogenerator and strain sensor based on transparent, long-term stable, and highly conductive gelatin-based organohydrogel. *Nano Energy* **95**, 106967 (2022).

41. F. M. Carvalho, P. Lopes, M. Carneiro, A. Serra, J. Coelho, A. T. de Almeida, M. Tavakoli, Nondrying, sticky hydrogels for the next generation of high-resolution conformable bioelectronics. *ACS Appl. Electron. Mater.* **2**, 3390–3401 (2020).

42. Y. Wang, S. Lee, H. Wang, Z. Jiang, Y. Jimbo, C. Wang, B. Wang, J. J. Kim, M. Koizumi, T. Yokota, T. Someya, Robust, self-adhesive, reinforced polymeric nanofilms enabling gas-permeable dry electrodes for long-term application. *Proc. Natl. Acad. Sci. U.S.A.* **118**, e2111904118 (2021).

43. X. Pan, Q. Wang, D. Ning, L. Dai, K. Liu, Y. Ni, L. Chen, L. Huang, Ultraflexible self-healing guar gum-glycerol hydrogel with injectable, antifreeze, and strain-sensitive properties. *ACS Biomater. Sci. Eng.* **4**, 3397–3404 (2018).

44. L. Han, K. Z. Liu, M. H. Wang, K. F. Wang, L. M. Fang, H. T. Chen, J. Zhou, X. Lu, Mussel-inspired adhesive and conductive hydrogel with long-lasting moisture and extreme temperature tolerance. *Adv. Funct. Mater.* **28**, 1704195 (2018).

45. S. Yang, Y. Zhang, T. Wang, W. Sun, Z. Tong, Ultrafast and programmable shape memory hydrogel of gelatin soaked in tannic acid solution. *ACS Appl. Mater. Interfaces* **12**, 46701–46709 (2020).

46. Y. Liu, L. Wang, Y. Mi, S. Zhao, S. Qi, M. Sun, B. Peng, Q. Xu, Y. Niu, Y. Zhou, Transparent stretchable hydrogel sensors: Materials, design and applications. *J. Mater. Chem. C* **10**, 13351–13371 (2022).

47. W. Y. Seow, G. Salgado, E. B. Lane, C. A. Hauser, Transparent crosslinked ultrashort peptide hydrogel dressing with high shape-fidelity accelerates healing of full-thickness excision wounds. *Sci. Rep.* **6**, 32670 (2016).

48. J. Xu, G. Wang, Y. Wu, X. Ren, G. Gao, Ultrastretchable wearable strain and pressure sensors based on adhesive, tough, and self-healing hydrogels for human motion monitoring. *ACS Appl. Mater. Interfaces* **11**, 25613–25623 (2019).

49. C. F. Guimarães, L. Gasperini, A. P. Marques, R. L. Reis, The stiffness of living tissues and its implications for tissue engineering. *Nat. Rev. Mater.* **5**, 351–370 (2020).

50. J. H. Kim, S. R. Kim, H. J. Kil, Y. C. Kim, J. W. Park, Highly conformable, transparent electrodes for epidermal electronics. *Nano Lett.* **18**, 4531–4540 (2018).

51. K. Yamagishi, I. Kirino, I. Takahashi, H. Amano, S. Takeoka, Y. Morimoto, T. Fujie, Tissue-adhesive wirelessly powered optoelectronic device for metronomic photodynamic cancer therapy. *Nat. Biomed. Eng.* **3**, 27–36 (2019).

52. Y. C. Choi, J. S. Choi, Y. J. Jung, Y. W. Cho, Human gelatin tissue-adhesive hydrogels prepared by enzyme-mediated biosynthesis of DOPA and Fe$^{3+}$ ion crosslinking. *J. Mater. Chem. B* **2**, 201–209 (2014).

53. Y. Su, N. Li, L. Wang, R. Lin, Y. Zheng, G. Rong, M. Sawan, Stretchable transparent supercapacitors for wearable and implantable medical devices. *Adv. Mater. Technol.* **7**, 2100608 (2022).

54. M. A. Zahed, M. Sharifuzzaman, H. Yoon, M. Asaduzzaman, D. K. Kim, S. Jeong, G. B. Pradhan, Y. D. Shin, S. H. Yoon, S. Sharma, A nanoporous carbon-mxene heterostructured nanocomposite-based epidermal patch for real-time biopotentials and sweat glucose monitoring. *Adv. Funct. Mater.* **32**, 2208344 (2022).

55. C. Wan, Z. Wu, M. Ren, M. Tang, Y. Gao, X. Shang, T. Li, Z. Xia, Z. Yang, S. Mao, In situ formation of conductive epidermal electrodes using a fully integrated flexible system and injectable photocurable ink. *ACS Nano* **17**, 10689–10700 (2023).

56. G. Hussain, J. Wang, A. Rasul, H. Anwar, M. Qasim, S. Zafar, N. Aziz, A. Razzaq, R. Hussain, J.-L. G. de Aguilar, Current status of therapeutic approaches against peripheral nerve injuries: A detailed story from injury to recovery. *Int. J. Biol. Sci.* **16**, 116–134 (2020).

57. D. B. MacDonald, C. Dong, R. Quatrale, F. Sala, S. Skinner, F. Soto, A. Szelényi, Recommendations of the international society of intraoperative neurophysiology for intraoperative somatosensory evoked potentials. *Clin. Neurophysiol.* **130**, 161–179 (2019).

58. R. Sharma, S. Joshi, K. Singh, A. Kumar, Visual evoked potentials: Normative values and gender differences. *J. Clin. Diagnostic Res.* **9**, CC12 (2015).

59. S. Lee, D. Sasaki, D. Kim, M. Mori, T. Yokota, H. Lee, S. Park, K. Fukuda, M. Sekino, K. Matsuura, Ultrasoft electronics to monitor dynamically pulsing cardiomyocytes. *Nat. Nanotechnol.* **14**, 156–160 (2019).

60. M. S. Brown, M. Mendoza, P. Chavoshnejad, M. J. Razavi, G. J. Mahler, A. Koh, Electronic-ECM: A permeable microporous elastomer for an advanced bio-integrated continuous sensing platform. *Adv. Mater. Technol.* **5**, 2000242 (2020).